Supporting Information for

Actuating Superparamagnetic Nanoparticle Monolayers

Edward P. Esposito, Hector Manuel Lopez Rios, Monica Olvera de la Cruz, Heinrich M. Jaeger

Monica Olvera de la Cruz, Heinrich M. Jaeger
E-mails: m-olvera@northwestern.edu, jaeger@uchicago.edu

This PDF file includes:

Supporting Information Text

Experiments

NP Synthesis. Super-paramagnetic Fe_3O_4 nanoparticles are synthesized by thermal decomposition following the Sun protocol (1). In order to achieve high-quality magnetic assemblies, it is essential to use this protocol, as other thermal decomposition syntheses seem to produce a high fraction of effectively non-magnetic particles due to the presence of magnetic anti-phase boundaries (2–4). All chemicals are purchased from Sigma-Aldrich and used as-ordered without further distillation. Fe(III)acac powder is ground to roughly 200 mesh with a mortar and pestle. Roughly 0.754 grams of the fine powder is added to a three neck reaction flask. 1.609 grams of oleylamine and 1.695 grams of oleic acid are added, together with 20 mL of octadecane. The air-free reaction uses a two-channel Schlenk line connected to a vacuum pump, or to the departmental N_2 line. The reaction flask is connected to the Schlenk line via a reflux chamber and the solution is heated under rough vacuum to 120 °C and held at that temperature for at least 1 hour while magnetically stirring, in order to degas and remove residual water. The reaction temperature is monitored with a temperature probe inserted through one of the necks of the flask. After gas bubbles no longer form in the reaction flask, the area around the flask and heating element is surrounded by several layers of aluminum foil to reduce the impact of high thermal gradients near the flask. The solution is then pressurized with N_2 to keep the reaction under positive pressure, heated to 200 °C and maintained at that temperature for 2 hours to nucleate Fe_3O_4 crystallites. The temperature is then increased to the reaction temperature of 320 °C at a rate of 5 °C/min, and maintained at 320 °C for 1 hr to grow the NP crystals.

It is not unusual for the reaction to bump (i.e. spurt suddenly into the reflux chamber for several seconds, with an accompanying drop in the reaction temperature of roughly 10-15 degrees). This phenomenon was either not encountered or not mentioned by others following this protocol. After a bump, the reaction typically takes several minutes to return to the set-point temperature of 320 °C. The reaction may bump several times over the course of an hour, but usually at least once. As far as we can tell, mid-reaction bumping and the accompanying drop in reaction temperature do not impact either the magnetic quality or the size and polydispersity of the synthesized particles, and therefore do not indicate that the synthesis must be abandoned.

After 1 hour the foil and heating mantle are removed, and the reaction is allowed to cool to room temperature under continued magnetic stirring. Once cool, the solution is poured into acetone and the particles are allowed to precipitate. Then the liquid phase is poured off and the particles are dissolved in toluene. To remove any excess reactants, the solution is added to ethyl alcohol, and centrifuged for typically 10-15 minutes until the particles precipitate, and the (now clear) liquid is again poured off. The particles are dispersed once more in toluene and can be used from this point on, or the washing process can be repeated. An aliquot of this solution is deposited on a Formvar coated copper TEM grid for inspection, and the particle size and polydispersity are evaluated from TEM images, taken using a FEI Spirit TEM, operating at 120 kV and using a LaB_6 filament. Unlike in Sun's paper (1), we were able to produce particles of core diameter 12.25 nm from the initial decomposition step, without using the formed crystallites as the seeds for subsequent thermal decomposition steps.

Sample Preparation and NP Self-Assembly. To make NP sheets for the deflection experiments, a bare copper TEM grid is placed on a microscope slide coated with PTFE tape. A 50 μL droplet of 18.2 MΩ ultrapure water is dropped onto the grid. A 1 μL droplet of nanoparticle solution is gently dropped onto the surface of the water droplet. Rapid evaporation of the toluene drives the particle assembly to form a monolayer film of the nanoparticles, visible as a faint brown tint at the water surface. The water droplet evaporates over a period of 4-5 hours, allowing the nanoparticle film to lower gently onto the copper grid. Samples are typically allowed to dry over night to ensure complete evaporation of the water.

NP Sheet Characterization. Some samples are used solely for TEM scans to determine the typical size and inter-particle separation of the NPs in the sheets. For this purpose, scans of the NP sheet over large portions of the TEM grid are performed at low magnification in order to locate and identify fully intact regions of the NP sheets, since partially supported sheets that have flexible or mobile parts move and deform due to the electron beam when imaged at higher magnifications. We also typically observe regions of the NP layer that consist of NP multilayers in order to avoid them in subsequent imaging. Once suitable regions of the TEM grid are identified, scans are taken at higher magnification (typically $11 - 18000\times$). Particle cores are identified and measured from the TEM images as dark circular regions on a lighter background using Hough transforms through MATLAB's built-in function `imfindcircles`. The TEM images are redisplayed with the identified circles superimposed in order to assess whether the algorithm identifies any spurious circles, and to ensure most if not all of the particles present in the image are found correctly. If particle identification was successful, we use the median and median absolute deviation of the typically asymmetric size distribution to characterize particle sizes and polydispersity. We then use the particle locations to calculate the particle radial distribution function $g(r)$, to characterize the inter-particle separation from the size and width of the first peak. Results from scans of different TEM grids (corresponding to different NP depositions according to the drop-casting described above) using the same stock of NPs (that is, nanoparticles synthesized and washed in the same batch) are aggregated to give averaged particle sizes and separation for a given stock. The particle size and separation are consistent for a given stock of NP solution, but differences in particle size are evident between particles from different syntheses, while variability in washing steps leads to variability in inter-particle separation. Consequently, the particle size and separation are characteristics of a single stock solution only. The size and separation values used throughout this work of 12.25 nm and 15.75 nm, respectively, were chosen for being the measured values of the NP stock actually used in the reported deflection

experiments. These values are typical of other of our NP stock solutions, for which particle sizes vary from 11-13 nm and particle separations vary from roughly 15-17 nm.

Samples are also used for AFM indentation experiments to characterize the typical stiffnesses of the sheets, following the experiments in (5). A Bruker Multi-Mode 8 AFM was used in single indentation mode with Bruker Scanasyst AFM probe tips made of Si_3N_4. The probe spring constant was calibrated thermally using the AFM, while the probe tip radius itself was measured separately by SEM (Zeiss Merlin, operating at 0.5 keV beam current), typically 4-8 nm. By indenting a fully intact NP sheet up to 200-300 nm, the cubic portion of the force-deflection curve was fit, resulting in nominal Young's moduli of 0.5-1.5 GPa. These Young's moduli are in a similar range as those extracted from the deflection experiments, as described in the main text. They are also nearly an order of magnitude softer than those measured in (5) for dodecanethiol-coated gold nanoparticles, likely due to the different ligand molecules. The NP sheets that partially tear free from the support structure cannot be indented in this way, since flexible NP sheets stick to the AFM probe tip (likely due to van der Waals interactions) and in doing so can tear completely free from the copper support. Therefore the Young's modulus of sheets used in the deflection experiments cannot be measured directly in this way.

Magnetic Deflections. For the deflection experiments, we identify segments of the NP layer that have torn free from the copper grid during the deposition process along two of the edges of one of the square holes to leave boundary conditions close to those used in the simulations. The sample is placed on a 3D printed sample holder, and the identified flaps are scanned using an Olympus LEXT OLS 5000 laser scanning confocal microscope using the 100x objective. For each flap, scans are performed at applied field strengths of $B = 0, 0.02, 0.04, 0.06, 0.08, 0.10, 0.12, 0.15, 0.19$ T in sequence. The height data are registered automatically using the optical images taken during each scan. Images and surface data are subsected to remove all but the flap under consideration and the surrounding square of the copper support. The copper region of the data is identified from the optical images, and the height data are leveled by subtracting the mean plane of the flat copper support region, and finally registered in the vertical direction by setting the copper region to the same height level. The region at the free corner of the flap is identified in each scan, and its (3D) displacement is calculated relative to the data at $B = 0$ T. Since the free portion of the flap may have slightly different boundary conditions from the simulations, instead of assuming the length of the free edge of the flap is just half the diagonal of the square, we calculate it for each sheet by identifying the "hinge" region, a line where the displacement across all scans is nearly zero, and measuring the orthogonal distance from the hinge to the free corner.

Magnetic field strengths of permanent magnets and of Halbach arrays are measured with an Allegro MicroSystems A1308-KUA-1-T linear Hall sensor connected to a regulated 5V source. With a sensitivity of 2 mV/Gauss, the nominal sensing range of the probe is 0-2500 Gauss. However the upper limits of this range showed a non-linear response that we did not characterize further. Instead, we simply assume that field strength measurements can only be taken up to 1900 Gauss. In order to characterize field gradients, two probes are joined face to face with adhesive, and the field gradient is taken as the difference in field strengths (i.e., by summing the two signals), divided by the separation between the two sensors, taken to be 0.56 mm (i.e., twice the nominal distance of 0.28 mm from the sensor to the surface of the A1308 according to the manufacturer's datasheet). The gradients in the fields from the permanent magnets is the primary source of uncertainty in the reported magnetic field strengths. The maximum measured gradient was 200 T/m. Assuming a fully saturated nanoparticle, such a field gradient could lead to a maximum force of 1.5×10^{-16} N. Note that the magnetic pressures arising from the dipole-dipole interactions as described in the main text are at least a factor of $10^2 - 10^3$ larger, even for the bulk particles. Therefore the external fields are always assumed uniform in experiment, especially once simulations revealed that external field gradients are not necessary to deflect the sheets. The gradients in the external field may provide some bias to cause an initially flat sheet to deflect preferentially in a particular direction, but the experimental sheets typically already have some initial deformation that biases their deflection.

Modeling

Independent Dipoles. The simplest model for a collection of superparamagnetic nanoparticles is the independent dipole model (IDM), used frequently when studying magnetic colloids, as well as in prior work by our group (6–8). In this model, the dipole magnetizations are a function of the external field strength only, so that $\mathbf{m}_{\mathrm{IDM}} = m(B_{\mathrm{ext}})\mathbf{B}_{\mathrm{ext}}/B_{\mathrm{ext}}$ for the assumed single particle magnetization function $m(B)$. We emphasize that in this model the dipoles are uniform throughout the system, since they all depend only on the external field. All are directed along the applied field, and all have the same strength of $m(B_{\mathrm{ext}})$. The IDM is often used together with a linear magnetization response function, namely the assumption that $m(B_{\mathrm{ext}}) = \chi B_{\mathrm{ext}}$ for a constant magnetic susceptibility χ. However, many authors implicitly use a non-linear magnetization response by allowing for a field-dependent susceptibility with $\mathbf{m} = \chi(B)\mathbf{B}$. Throughout the work discussed here we assume the magnetization response follows the Langevin function $m(B) = m_{\mathrm{sat}}\mathcal{L}(B/B_{\mathrm{sat}}) = m_{\mathrm{sat}}(\coth(B/B_{\mathrm{sat}}) - B_{\mathrm{sat}}/B)$. In principle, we could then define a susceptibility $\chi(B) = m_{\mathrm{sat}}\mathcal{L}(B/B_{\mathrm{sat}})/B$ in the same way, but we do not make further use of the susceptibility. In all of these cases, regardless of the magnetization function assumed, the dipole moments only depend on the external field.

Mutually Dependent Dipoles. When the field due to the induced dipoles is appreciable relative to the external field, the total field experienced by a dipole cannot be approximated well by the externally applied field alone. This case is best described by the mutual dipole model (MDM) (9–12) in which the induced magnetizations depend now on the total field $\mathbf{B}_{\mathrm{tot}} = \mathbf{B}_{\mathrm{dip}} + \mathbf{B}_{\mathrm{ext}}$ through $\mathbf{m}_{\mathrm{MDM}} = m(B_{\mathrm{tot}})\mathbf{B}_{\mathrm{tot}}/B_{\mathrm{tot}}$. Although this model is more accurate than the IDM, it can substantially increase the complexity of the problem. Since the dipole field at the location of a given particle i, namely

$\mathbf{B}_{\rm dip}(\mathbf{r}_{\rm i}) = \sum_{\rm j\neq i} \frac{\mu_0}{4\pi r_{\rm ij}}[3(\hat{\mathbf{r}}_{\rm ij}\cdot\mathbf{m}_{\rm j})\hat{\mathbf{r}}_{\rm ij} - \mathbf{m}_{\rm j}]$, includes a sum over all other particles, the total dipole energy $U_{\rm dip} = -\frac{1}{2}\sum_{\rm i}\mathbf{m}_{\rm i}\cdot\mathbf{B}_{\rm dip}(\mathbf{r}_{\rm i})$ includes a double sum over all of the particles, and so the complexity of the energy computation scales (naively) as $\mathcal{O}(N^2)$. There are algorithmic techniques to reduce the complexity of dipole sums to $\mathcal{O}(N^{3/2})$ or even $\mathcal{O}(N\log N)$, specifically the P3M method(13–15), but these are known to introduce potentially sizable errors into the values of computed forces, and so we did not exploit these methods.

Semi-Independent Dipoles. Optimizing the dipole-dipole energy requires calculating the energy function many times. For simple magnetization functions (indeed, for linear magnetization) the problem may be tractable even for large systems. However, for non-linear magnetization functions, optimizing large systems becomes very time consuming. To reduce the computation time, we have found it useful to introduce a model lying somewhere between the IDM and MDM, calling it the semi-Independent Dipole Model (sIDM), in which $\mathbf{m}_{\rm sIDM} = m(B_{\rm ext})\mathbf{B}_{\rm tot}/B_{\rm tot}$. The IDM assumes that the dipole magnitudes and direction are both determined by the applied field only, while the MDM assumes that dipole magnitudes and directions are determined both by the applied field and the field arising from all of the other dipoles. In the sIDM, the dipole magnitudes are determined by the external field only, but the dipole directions are determined by the total field arising from all of the other dipoles as well as the applied field. The sIDM avoids calculating the non-linear magnetization function of the total field, thereby avoiding the most time consuming computations, while nevertheless preserving some information of the total field by using it to determine the dipole moment directions.

Comparing the Dipole Models. Because of how time-consuming the computations are when using the full MDM with non-linear magnetization function, the simplified models would generally be preferable if they predicted deflections similar to those from the MDM. We found that the IDM introduces sizable errors in deflection when compared with the MDM, as shown in Fig. (S1) where $\delta_{\rm IDM}/L$ is represented by the yellow circles and $\delta_{\rm MDM}/L$ is represented by the black circles. In particular, the IDM predicts limited deflection for a flat sheet at low external fields because the dipole moments are all normal to the initially flat metastable state, while the forces are small. It also over-predicts the deflection at large external field strengths because the dipoles all have the same dipole moment strength. The IDM therefore should only be used for systems with much larger inter-particle separation than ours. The sIDM on the other hand produces nearly the correct deflection, differing only slightly from the MDM deflections at lower field strengths. The sIDM predicts the deflection well because it gives a good estimate of the magnetization direction, shown as a function of the local sheet orientation in Fig. (S2). The differences with the MDM become appreciable only for flat orientations where the sIDM curves tend to intersect the y-axis (in contrast with Fig. (3) from the main text). However, the magnetization and magnetic pressure calculated from the sIDM also show unphysical discontinuities, visible as the lines and points in the upper images of Figs. (S3), (S4), and (S5). We suspect therefore that the sIDM may rely on unphysical assumptions. Still, because it yielded nearly the correct deflection, we found it useful as an intermediate step in the simulation in order to quickly generate an initial guess for the mechanical deformation and for the magnetization state. These initial guesses were then refined using the computationally costly MDM.

In all such models, the nanoparticles are assumed to be uniformly magnetized spheres, such that they can be considered in terms of point dipoles. When polarizable spheres are very closely spaced, uniform magnetization stops being a good assumption because the local field has appreciable gradients at the particle scale. Further refinements to the modeling would include higher-order multipole moments (10, 11). However, this greatly increases the complexity of the model (especially considering the size of our system, $N = 22680$ particles in the MD simulation). Because we wanted to focus on the impact of the non-linear magnetization function, and because the experimental nanoparticle cores are separated by $r/D = 1.29$, a regime for which Li et al. demonstrate that there are only small differences between the strengths of forces from MDM and from higher-order multipolar modeling, we did not pursue these refinements.

Magnetization Directions and Sheet Stiffness. In Fig. 3A of the main text, we reported the magnetization direction θ_m as a function of the local surface normal direction θ_n (both angles being defined with respect to the direction of the applied field). Using the simulations of a 1 GPa sheet, surface normals and magnetization vectors of the equilibrated sheets were calculated at each applied field strength. At a given field strength, the values of θ_m observed for each angle θ_n in the sheet were averaged to produce the reported point. Such results may be affected by the sheet's overall configuration. For example, a sheet with a large deflection has many more regions with large θ_n than a sheet with a small deflection. To evaluate whether these results are strongly affected by the sheet's configuration, we did the same analysis using simulations of sheets with different Young's moduli, $E = 0.5 - 5$ GPa, reasoning that softer sheets will have more regions at large θ_n and could therefore show different behavior. The results are shown in Fig. S6, where the color of the dots now represents the Young's modulus of the sheet it was calculated from, while the dashed lines represent the function $\theta_m(\theta_n)$ reported in the main text (fitted to the data points from the E = 0.5 GPa simulation to ensure a good fit to the $B_{\rm ext} = 0.02$ T data points), with darker lines corresponding to weak fields and brighter lines corresponding to strong fields. Indeed the stiffer sheets stay mostly flat while the softer sheets bend quite a bit, as can be seen from the fact that the lighter points (from stiffer sheets) populate the regions of small θ_n while the darker points (from softer sheets) extend into the region of high θ_n. But it is also striking that the points, whatever their color (ie whatever the stiffness of the simulated sheet), seem to trace the very same lines. Therefore, the reported behavior of $\theta_m(\theta_n)$ is not heavily sensitive to the configuration of the sheets, which can be very different between the softest and the stiffest sheets at a given field strength, and is therefore somewhat generic. These results give us confidence that the same magnetization functions can be used freely to describe the experimental sheets, which indeed vary in stiffness across this range. Moreover, since the form of these functions is not impacted by the substantially different configurations of soft and stiff sheets, we believe

they can be used as good approximations to the magnetization behavior of NP sheets in 3D configurations more complex than an initially flat sheet, provided the curvatures are not too extreme (i.e. that they do not approach the single particle scale) and that they have the same average inter-particle distances and magnetic properties.

Ordering Effects. To check the effects of disorder on sheet deflection, we introduced random disorder into 1 GPa sheets using the sIDM in order to simulate enough different configurations to sample the randomness (rather than the full MDM as we used elsewhere in this work). Disorder is generated in two different ways: (1) randomly deactivating the magnetic dipoles of a fraction of the particles, or (2) randomly deleting a fraction of the particles. In (1), the deactivated particles do not interact magnetically, but still interact elastically with their neighbors, while in (2) the deleted particles no longer interact either magnetically or elastically. Both types of disorder can be present in the experimental sheets, but we observe that any holes with missing NPs are almost always filled with free oleic acid ligands, preserving the local elastic connections in a situation closer to (1). In addition, although the Sun protocol reduces the fraction of non-magnetic NPs as mentioned in the section above on NP synthesis, there are still likely some non-magnetic NPs present, a situation that is captured directly by deactivating dipoles.

As an example, we show the change in end deflection of simulated defective sheets relative to the deflection of a pristine sheet for a vertical external magnetic field $B_{\text{ext}} = 0.12$ T in Fig. S7. The blue points show that sheets with deactivated dipoles deflected less than the pristine sheet when more dipoles were deactivated. The deflection is reduced because these sheets retain the same bending stiffness as the pristine sheet (since no elastic interactions were removed), while the magnetic pressure is reduced when compared with a pristine sheet because the deactivated dipoles no longer experience magnetic forces. Deflecting less might be interpreted as an increase in the apparent stiffness for a given external field. In contrast, the red points show that sheets with deleted particles deflect more than the pristine sheet as the fraction of deleted particles increases. In this case, the deleted NPs correspond to holes which are known to reduce the effective stiffness of elastic sheets (16). This effective softening due to the holes is apparently a more significant effect than the reduced magnetic pressure due to the missing dipoles. We believe both types of disorder are present in the experimental sheets, although we believe that missing dipoles are more common than elastic holes. There are certainly other types of disorder in the experimental sheets (point defects, grain boundaries, etc.), that are likely to have a strong effect as well, and which we did not address here. But these results show that disorder can either enhance or reduce the apparent stiffness of the sheets, and we believe the variability of stiffness in the experimental sheets as extracted from the deflection curves can be explained in part by disorder.

Size Effects. The force between a pair of dipoles is given explicitly by

$$\mathbf{F}_{\text{ij}} = \frac{3\mu_0}{4\pi r_{\text{ij}}^4}[(\mathbf{m}_{\text{i}} \cdot \hat{\mathbf{r}}_{\text{ij}})\mathbf{m}_{\text{j}} + (\mathbf{m}_{\text{j}} \cdot \hat{\mathbf{r}}_{\text{ij}})\mathbf{m}_{\text{i}} + (\mathbf{m}_{\text{i}} \cdot \mathbf{m}_{\text{j}})\hat{\mathbf{r}}_{\text{ij}} - 5(\mathbf{m}_{\text{i}} \cdot \hat{\mathbf{r}}_{\text{ij}})(\mathbf{m}_{\text{j}} \cdot \hat{\mathbf{r}}_{\text{ij}})\hat{\mathbf{r}}_{\text{ij}}].$$

Considering an infinite sheet with uniform magnetization $\mathbf{m}$, we can compute the total force on particle i (assumed to be located at the origin) by integrating the force expression over the plane:

$$\begin{aligned}\mathbf{F}_{\text{i}} &= \frac{3\mu_0 m^2}{4\pi^2 r_0^2}\int_{r_0}^{L} \mathrm{d}r \int_0^{2\pi} \mathrm{d}\phi \, \frac{2(\hat{\mathbf{m}} \cdot \hat{\mathbf{r}})\hat{\mathbf{m}} + (1 - 5(\hat{\mathbf{m}} \cdot \hat{\mathbf{r}})^2)\hat{\mathbf{r}}}{r^3} \\ &= \frac{\mu_0 m^2}{4\pi^2 r_0^2}\left(\frac{1}{r_0^2} - \frac{1}{L^2}\right)\int_0^{2\pi} \mathrm{d}\phi \, [2(\hat{\mathbf{m}} \cdot \hat{\mathbf{r}})\hat{\mathbf{m}} + (1 - 5(\hat{\mathbf{m}} \cdot \hat{\mathbf{r}})^2)\hat{\mathbf{r}}\end{aligned}$$

where $L \to \infty$ in the limit. For a large plate, the total force on a particle therefore goes like $\frac{\mu_0 m^2}{4\pi^2 r_0^4}$ with an error due to a finite cutoff that is $\mathcal{O}((\frac{r_0}{L})^2)$. For the simulated sheets, the force scale is $F \approx 2.7 \times 10^{-13}$ N, with an error of $(r_0/L)^2 \approx 3 \times 10^{-5}$.

Note that for a sheet with uniform magnetization, the direction of the force does not depend on the finite cutoff length L, depending rather only on the direction of $\mathbf{m}$. Moreover, for a flat sheet with uniform magnetization, the force will always be in-plane, since the integral of the term proportional to $\hat{\mathbf{m}}$ is zero. Therefore, the only way such a sheet can be subjected to out-of-plane forces is if there is some curvature in the sheet, so that $\hat{\mathbf{r}}$ is sometimes out-of-plane.

Fitting Functions. The function in Eq. **3** was found by fitting simulated deflection curves using MATLAB's built-in `fit` function. We observed that any such function should have some initial curvature, and that it should saturate for high fields. Several types of function with these properties interpolated the deflection curves well over the range of field values used in the main text (0-0.25 T). Note that any saturating function that is linear at the origin can be adapted for this purpose by squaring it (for instance $\tanh^2(x)$ or $\mathcal{L}^2(x)$). However, the different functions generally had rather different saturated values (differing by up to 30%), despite interpolating the data similarly well. Because of the differing saturated values, we found that data points following the various hypothesized curves could be differentiated reliably by our fitting routine with the inclusion of two additional points at very high fields, 0.5 T and 1 T. When we performed additional simulations (for $E = 1$ GPa) with these two extra points included, the function in Eq. (3) in the main text (with $\alpha = 1.8$) was the only one fitting all of the simulated deflections.

Simulation Parameters

NP Sheet Elasticity. We follow the Seung-Nelson model (17) to convert from the elasticity of a continuum sheet to a triangular lattice of discrete points representing the nanoparticles. We assume isotropic elasticity within the sheets as all points comprise a perfect triangular lattice. Points on this lattice are elastically constrained through two types of inter-particle interactions: (I) a pairwise stretching potential $u_s(r) = \frac{1}{2}k\,(r - r_0)^2$ between nearest neighbors, with an equilibrium distance r_0 and stretching constant k; and (II) a four body out-of-plane bending potential $u_b(\theta) = \kappa\,[1 - \cos(\theta - \theta_0)]$ that penalizes deviations from an equilibrium angle θ_0 between neighboring triangular facets sharing an edge, weighted by a bending constant κ. These potentials together model isotropic elastic thin plates by mapping a physical sheet's 2D Young's modulus $E^{2D} = Et$ and bending rigidity $Y = \frac{Et^3}{12(1-\nu^2)}$ respectively to the stretching constant $k = \frac{\sqrt{3}}{2}E^{2D}$ and out-of-plane bending constant $\kappa = \frac{2}{\sqrt{3}}Y$ (17, 18). E, t, and ν respectively corresponding to the sheet's Young's modulus, thickness, and Poisson ratio. For the values of all parameters used in the simulations, see Table (S1). To replicate the clamped boundary conditions of the experimental sheets, we hold nanoparticles within two diameters of the x- and y- axes fixed (to ensure zero displacement and zero slope along those edges), with the other two edges free.

MD Simulations. We use mass, length and energy as our set of fundamental units in the simulation, and scale them by the average mass and diameter of the experimental magnetic particles, and the magnetic dipole-dipole energy of a pair of parallel magnetic dipoles separated by r_0. All simulations are integrated using the NVT ensemble with a Langevin thermostat at $T = 0$ K and damping parameter $\gamma = 0.9$. This damping value does not represent any physical friction but was chosen out of convenience to suppress fluctuations about the equilibrium configuration, and so to reduce the number of steps needed to reach the equilibrium state. Furthermore, we choose athermal simulations because thermal fluctuations will not qualitatively impact the mechanical equilibrium configuration of the sheets at different external magnetic fields. All simulated sheets begin in a flat configuration. Because flat sheets are metastable under an external magnetic field normal to it, we evolve the sheet for the first 200 time steps using an offset external magnetic field $\hat{\mathbf{B}_{\text{ext}}} = 0.0101\hat{i} + 0.0101\hat{j} + 0.9999\hat{k}$ to generate a non-flat configuration, before using the true field we wish to apply. For instance, an initially flat sheet in a magnetic field $\mathbf{B} = B_{\text{ext}}\hat{\mathbf{z}}$ would evolve for the first 200 time steps under the offset field $\mathbf{B} = B_{\text{ext}}(\frac{\sqrt{2}}{2}\sin\theta_{\text{off}}\hat{\mathbf{x}} + \frac{\sqrt{2}}{2}\sin\theta_{\text{off}}\hat{\mathbf{y}} + \cos\theta_{\text{off}}\hat{\mathbf{z}})$. We also calculate dipole magnitudes and orientations using the sIDM for the same first 200 time steps, no matter the final external field orientation. This accelerates our simulations as it quickly gives a sheet configuration closer to the equilibrated state before transitioning to the more expensive MDM. Initiating the MDM from a deflected configuration instead of a flat configuration does not impact the final deflected state. After the initial 200 time steps, we revert to the MDM to calculate dipole magnitudes and orientations, and to a fully vertical external magnetic field if an offset initial field was used. We evolve the sheet's configuration while solving for the dipoles after every time step until the following conditions are satisfied: the difference of the total elastic energy between the new configuration and the previous one is less than 0.5 scaled energy units, the maximum magnetization difference between the new configuration and the previous one is less than 10^{-4} scaled magnetization units, and the speed of the free corner particle of the new configuration is less than 10^{-3} scaled speed units.

Finally, solving the dipole magnitudes and orientations using the MDM requires a non-linear solver. We use the Nonlinear Generalized Minimum Residual (NGMRes) method (19) as implemented in the the Python wrapper version of the Portable, Extensible Toolkit for Scientific Computation (PETSc) (20). Interestingly, the non-linearity of the MDM varies as a function of the magnitude of the external magnetic field as solutions below a certain tolerance were difficult to obtain for low magnetic fields. This led us to use two different tolerances for the solver based on the magnitude of the external field. For $|\mathbf{B}_{\text{ext}}| \leq 0.04$ T we used the tolerance of 5×10^{-3}, and otherwise 5×10^{-6}.

Parameter	Value
Length unit	12.25 nm
Mass unit	9.066×10^{-21} kg
Energy unit	1.3462×10^{-20} J
Equilibrium distance r_0	15.75 nm
m_{sat}	7.7×10^{-18} emu
B_{sat}	$0.03\dot{3}$ T
Young's Modulus E	{0.5,1.0,1.5,2.0,3.0,5.0} GPa
Poisson ratio ν	1/3
Sheet thickness t	12.25 nm

Table S1. Molecular dynamics simulation parameters used

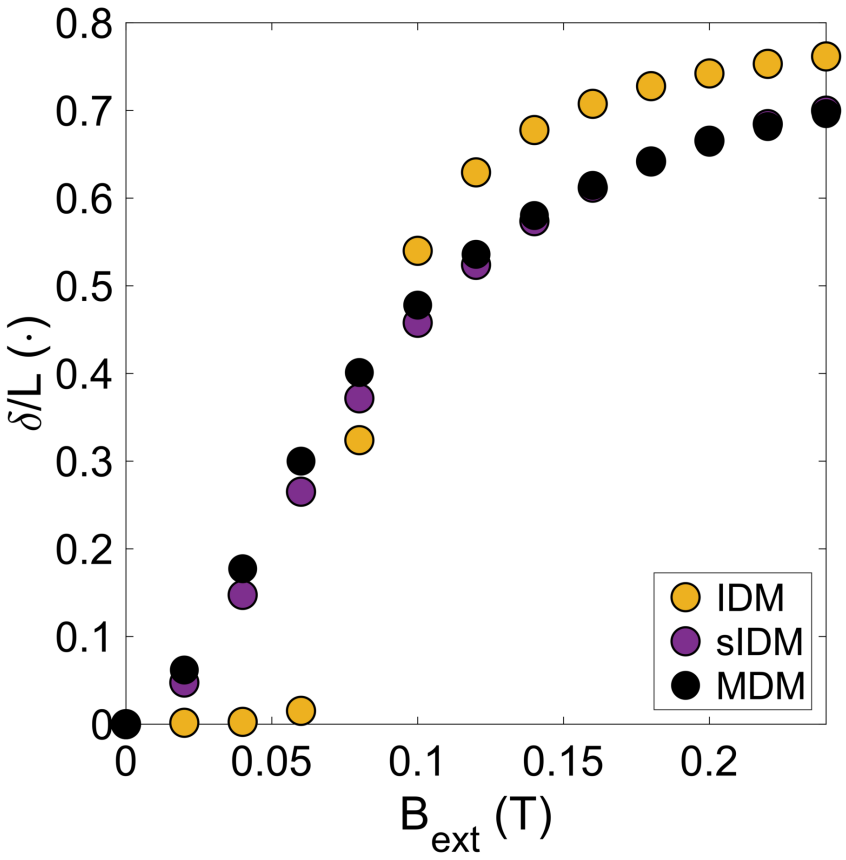

Fig. S1. NP Sheet deflection for different dipole models. Using different dipole models leads to different deflections δ at a given applied field. The difference between the IDM (yellow) and MDM (black) is very notable. The maximum deflection for the IDM is larger, and the sheet does not deflect at all until the external field exceeds some threshold value. The differences between the sIDM and the MDM are more subtle, only being apparent small and intermediate field values. This is why our simulations used the sIDM to provide an initial guess of the configuration before refining it with the MDM. All deflection curves plotted here are based on simulations using a 1 GPa Young's modulus.

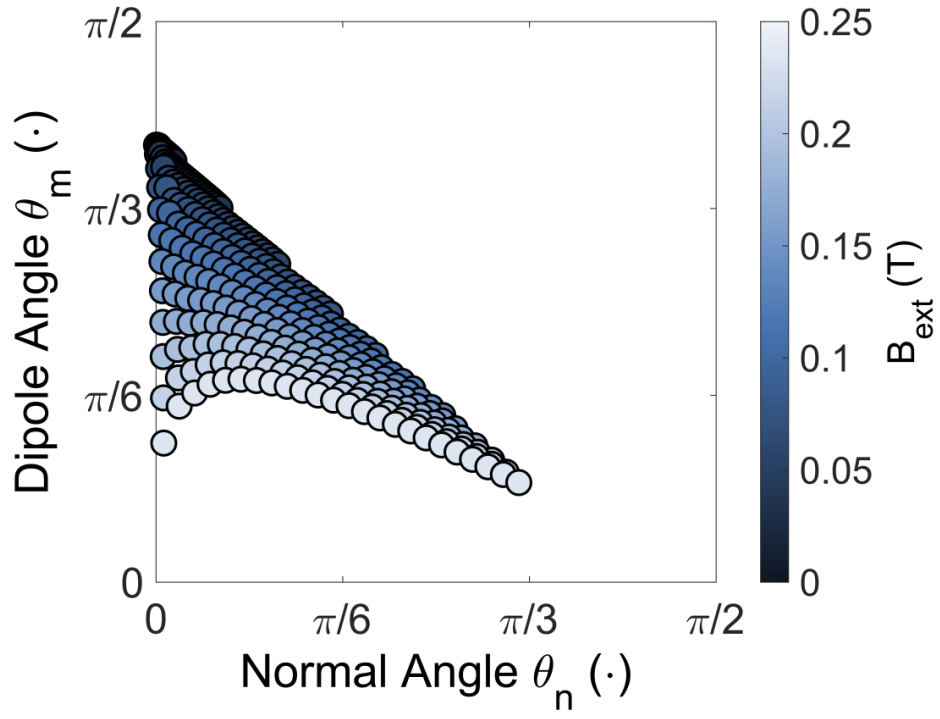

Fig. S2. Magnetic response of actuated sheets using sIDM. Magnetization angle $\theta_{\mathrm{m}}(\theta_{\mathrm{n}})$ curves using sIDM for a sheet with Young's modulus 1 GPa, actuated by external magnetic fields $\mathbf{B}_{\mathrm{ext}} = \mathrm{B}_{\mathrm{ext}}\,\hat{z}$ with field strength indicated by the color bar. The sIDM $\theta_{\mathrm{m}}(\theta_{\mathrm{n}})$ curves are similar to the results based on MDM when θ_{n} is moderately large so that the induced magnetization approaches the plane of the sheet. By contrast, θ_{m} does not approach zero as $\theta_{\mathrm{n}} \to 0$, meaning that a flat sheet in a vertical field will neither magnetize in-plane nor in the applied direction for the sIDM, but rather at some intermediate value. This fact is probably responsible for the discontinuities appearing in plots S3 - S5.

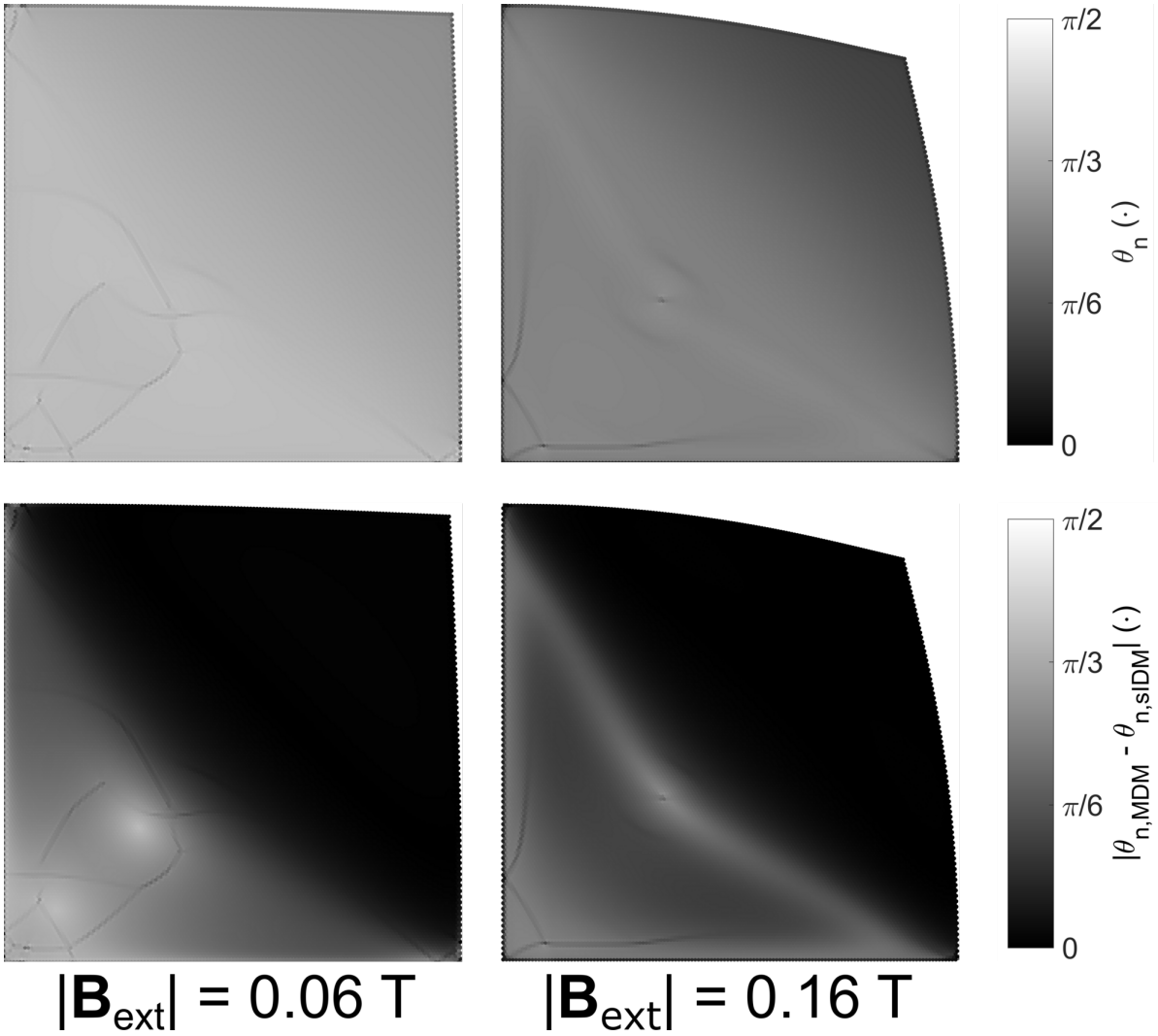

Fig. S3. Differences between $\theta_{n,MDM}$ and $\theta_{n,sIDM}$. The direction of the dipole moments is shown in the top row for low and high fields (left and right, respectively). As compared with the moment directions for the MDM presented in the main paper, the distribution here is more uniform throughout the sheet. Also visible are lines and points where the direction changes dramatically from one particle to its neighbor, features of the sIDM we believe are unphysical. The bottom row displays the same data as the difference between the directions calculated using the MDM and the sIDM, demonstrating that the difference is small in the free portion of the sheet but quite large in the fixed portion.

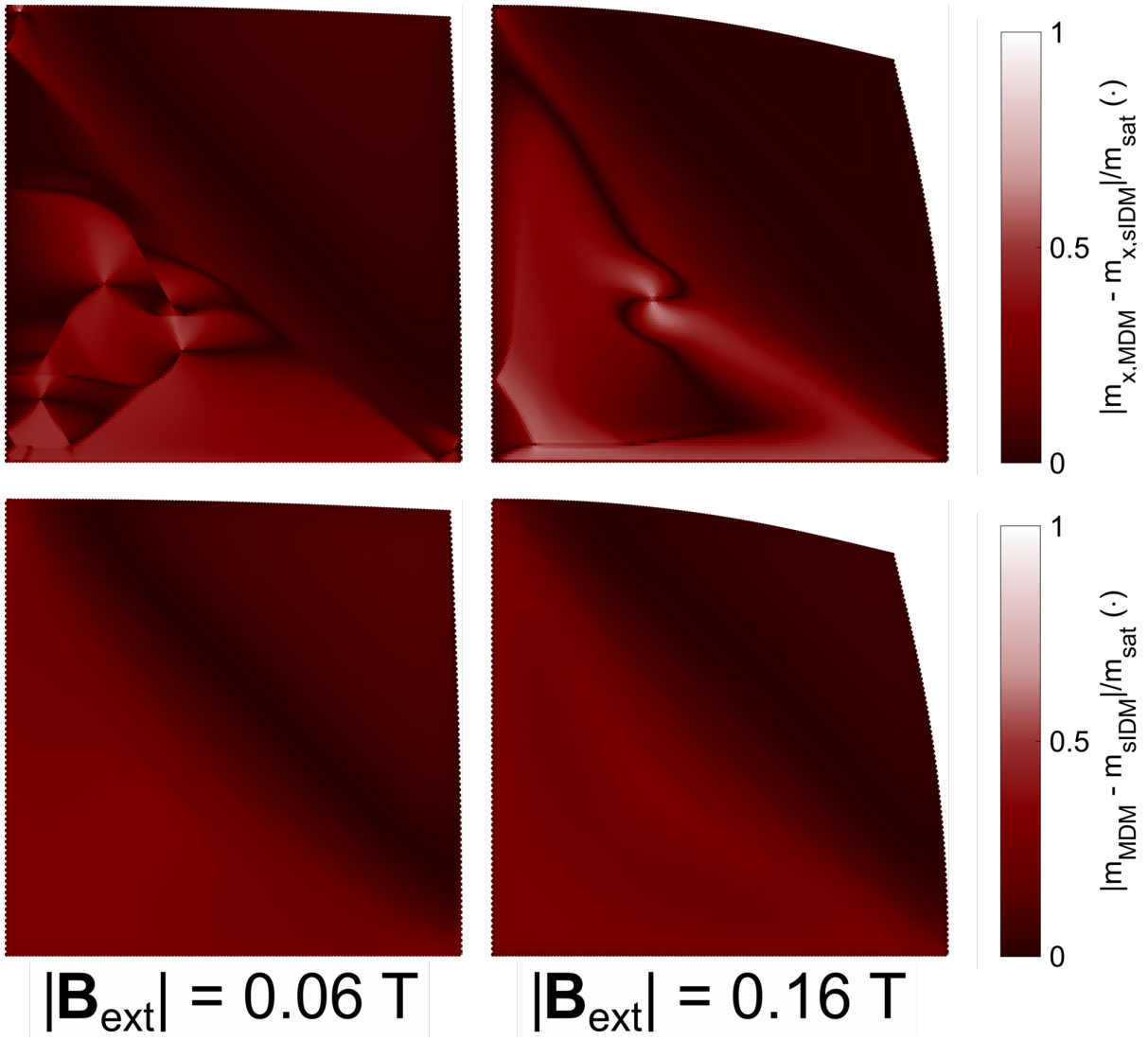

Fig. S4. Differences between m_{MDM} and m_{sIDM}. The top row shows the difference between one component of the dipole moments calculated via the sIDM and the MDM, at low field on the left and high field on the right. The plots shows this for the x component; the y and z components exhibit qualitatively similar differences). The images demonstrate the striking magnetization discontinuities present when using the sIDM. The bottom row displays the difference in the total magnetization between the two models.

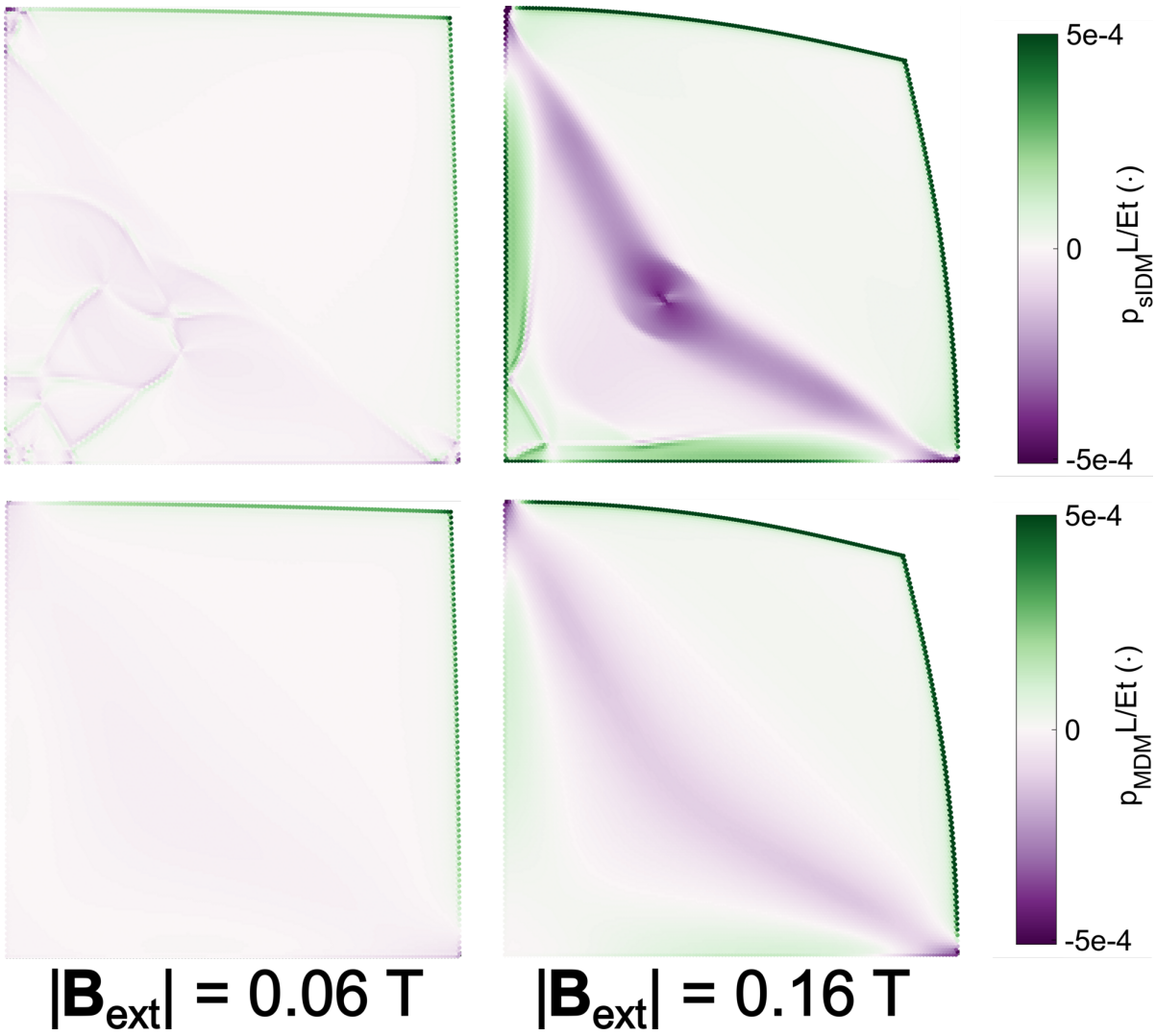

Fig. S5. Difference between p_{MDM} and p_{sIDM}. The top row displays the pressure distributions using the sIDM, both for low and high fields. The bottom row plots the pressure distributions using the MDM, as also shown in Fig. 4C. The differences in magnetization vectors between the MDM and sIDM lead to only small differences in these pressure distributions, which is why the deflection curves turn out to be so similar. Especially notable, given the small difference between the end deflections, is that the strength of the magnetic forces is larger in the sIDM particularly in the interior of the sheet, along the sheet's crease.

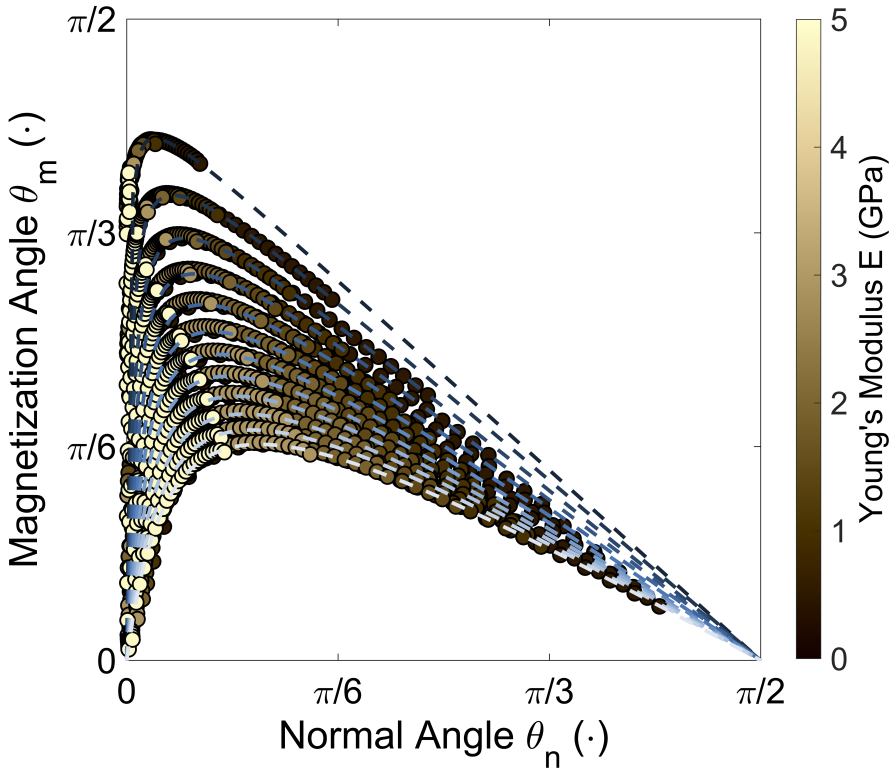

Fig. S6. Magnetization direction for different sheet stiffnesses. As in Fig. 3A in the main text, the dots show the average of the distribution of single particle magnetization directions θ_{m} for given θ_{n} from molecular dynamics (MD) simulations. Distributions of θ_{m} for given θ_{n} were obtained in simulated sheets actuated by different external field magnitudes. The angles θ_m and θ_n represent the deviations of the particle magnetic moments and of the local sheet normal from the direction of the applied field, respectively. While all data in Fig. 3A were obtained from equilibrated sheet configurations for a fixed Young's modulus (1 GPa), here we use sheets with Young's moduli over the range of $E = 0.5 - 5$ GPa, with darker dots representing data from softer sheets and lighter dots from stiffer sheets. The dashed curves represent the function $\theta_m(\theta_n)$ from Eq. (5) in the main text, fit to the data for $E = 0.5$ GPa. Each line represents a different external field strength, ranging from 0.02 T (top, darkest line) to 0.24 T (bottom, lightest line) as in Fig. 3A. For a given field strength, θ_{m} seems to trace the same curve regardless of the sheet stiffness, merely sampling different regions of the same curves based on how much the sheet deflects.

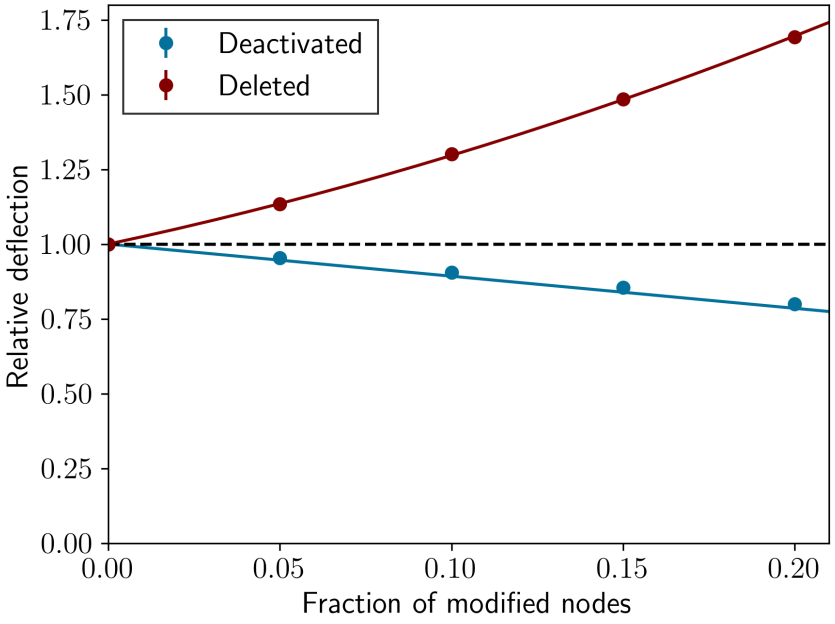

Fig. S7. Impact of defects on sheet deflection. Sheets with varying types and amounts of disorder are exposed to an external magnetic field $\mathbf{B}_{\mathrm{ext}} = 0.12\hat{z}$, and their deflections are compared with that of a pristine sheet (black dashed line). Disorder is modeled either by randomly deactivating a fraction of magnetic dipoles in the simulated sheet without removing any elastic connections (blue points), or by randomly deleting a fraction of particles and their elastic connections, thereby creating holes in the sheet (red points). Data points represent the average of five different simulations for the deactivated and four for the deleted types of disorder, and all error bars are smaller than the size of the data points. Solid lines are guides to the eye.

References

1. Shouheng Sun, Hao Zeng, David B. Robinson, Simone Raoux, Philip M. Rice, Shan X. Wang, and Guanxiong Li. Monodisperse MFe $_2$ O $_4$ (M = Fe, Co, Mn) Nanoparticles. *J. Am. Chem. Soc.*, 126(1):273–279, 2004.
2. Zlatko Nedelkoski, Demie Kepaptsoglou, Leonardo Lari, Tianlong Wen, Ryan A. Booth, Samuel D. Oberdick, Pedro L. Galindo, Quentin M. Ramasse, Richard F. L. Evans, Sara Majetich, and Vlado K. Lazarov. Origin of reduced magnetization and domain formation in small magnetite nanoparticles. *Sci Rep*, 7(1):45997, 2017.
3. William W. Yu, Joshua C. Falkner, Cafer T. Yavuz, and Vicki L. Colvin. Synthesis of monodisperse iron oxide nanocrystals by thermal decomposition of iron carboxylate salts. *Chemical Communications*, (20):2306–2307, 2004.
4. Jongnam Park, Kwangjin An, Yosun Hwang, Je-Geun Park, Han-Jin Noh, Jae-Young Kim, Jae-Hoon Park, Nong-Moon Hwang, and Taeghwan Hyeon. Ultra-large-scale syntheses of monodisperse nanocrystals. *Nature materials*, 3(12):891–895, 2004.
5. Yifan Wang, Pongsakorn Kanjanaboos, Sean P. McBride, Edward Barry, Xiao-Min Lin, and Heinrich M. Jaeger. Mechanical properties of self-assembled nanoparticle membranes: stretching and bending. *Faraday Discuss.*, 181:325–338, 2015.
6. Joshua M Dempster, Pablo Vázquez-Montejo, and Monica Olvera de la Cruz. Contractile actuation and dynamical gel assembly of paramagnetic filaments in fast precessing fields. *Physical Review E*, 95(5):052606, 2017.
7. Chase Austyn Brisbois, Mykola Tasinkevych, Pablo Vázquez-Montejo, and Monica Olvera De La Cruz. Actuation of magnetoelastic membranes in precessing magnetic fields. *Proc. Natl. Acad. Sci. U.S.A.*, 116(7):2500–2505, February 2019. ISSN 0027-8424, 1091-6490. . URL https://pnas.org/doi/full/10.1073/pnas.1816731116.
8. Chase Austyn Brisbois and Monica Olvera De La Cruz. Locomotion of magnetoelastic membranes in viscous fluids. *Phys. Rev. Research*, 4(2):023166, 2022.
9. Eric E. Keaveny and Martin R. Maxey. Modeling the magnetic interactions between paramagnetic beads in magnetorheological fluids. *Journal of Computational Physics*, 227(22):9554–9571, 2008.
10. Di Du, Frank Toffoletto, and Sibani Lisa Biswal. Numerical calculation of interaction forces between paramagnetic colloids in two-dimensional systems. *Phys. Rev. E*, 89(4):043306, 2014.
11. Di Du and Sibani Lisa Biswal. Micro-mutual-dipolar model for rapid calculation of forces between paramagnetic colloids. *Phys. Rev. E*, 90(3):033310, 2014.
12. Zachary M Sherman, Dipanjan Ghosh, and James W Swan. Field-Directed Self-Assembly of Mutually Polarizable Nanoparticles. *Langmuir*, 34(24):7117–7134, 2018.
13. Juan J. Cerdà, V. Ballenegger, O. Lenz, and C. Holm. P3M algorithm for dipolar interactions. *The Journal of Chemical Physics*, 129(23):234104, 2008.
14. Markus Deserno and Christian Holm. How to mesh up Ewald sums. I. A theoretical and numerical comparison of various particle mesh routines. *The Journal of Chemical Physics*, 109(18):7678–7693, 1998.
15. Markus Deserno and Christian Holm. How to mesh up Ewald sums. II. An accurate error estimate for the particle–particle–particle-mesh algorithm. *The Journal of Chemical Physics*, 109(18):7694–7701, 1998.
16. Jiayue Tao, Hesameddin Khosravi, Vishrut Deshpande, and Suyi Li. Engineering by cuts: How kirigami principle enables unique mechanical properties and functionalities. *Advanced Science*, 10(1):2204733, 2023.
17. H. S. Seung and David R. Nelson. Defects in flexible membranes with crystalline order. *Phys. Rev. A*, 38(2):1005–1018, 1988.
18. Martin Ostoja-Starzewski. Lattice models in micromechanics. *Applied Mechanics Reviews*, 55(1):35–60, 2002.
19. Peter R. Brune, Matthew G. Knepley, Barry F. Smith, and Xuemin Tu. Composing scalable nonlinear algebraic solvers. *SIAM Review*, 57(4):535 – 565, 2015.
20. Lisandro D. Dalcin, Rodrigo R. Paz, Pablo A. Kler, and Alejandro Cosimo. Parallel distributed computing using python. *Advances in Water Resources*, 34(9):1124 – 1139, 2011.